



# Modeling Parameters for Finite Element Simulation of Residual Stress in Cold Spray and the Stress Evolution and Distribution

Fanchao Meng<sup>1</sup> · Xiaping Fan<sup>1</sup> · Zonglin Chi<sup>1</sup> · Shuying Chen<sup>1</sup> · Xin Chu<sup>2</sup>

Submitted: 25 October 2022 / in revised form: 18 July 2023 / Accepted: 19 July 2023 / Published online: 9 August 2023  
© ASM International 2023

**Abstract** Residual stress is an important factor that affects the properties of cold spray coatings. The study performed 2D single-, 3D single-, and 3D multiple-particle finite element simulations based on the Eulerian method, and hole drilling measurements to study residual stress in cold-sprayed copper coatings. The study examined how the basic modeling parameters affect residual stress in the 2D system. It found that the mesh size, substrate dimension, and simulation duration change the residual stress; while material failure does not have much effect because failure is localized. It also found that thermal softening, which occurs when the initial temperature and/or plastic deformation increase, helps to reduce the residual stress. In addition, the residual stress along the axisymmetric axis of the particle changes from being compressive at first to being compressive-tensile-compressive along the through-depth thickness direction with the interfacial stress being tensile that mainly originates from friction shear of the interfacial layers. For the 3D single-particle simulations, the average residual stress to the through-depth thickness shows tension to compression transition and is similar to the 2D cases. For the 3D multiple-particle simulations, the residual stresses in the coatings/substrate are all

compressive because of the repeated and strong impact of the particles, which agree with the experimental measurements. The study also found that the compressive stresses decrease when the coating thickness increases because of more plastic deformation-induced thermal softening. This paper clarifies the effects of Eulerian-based finite element parameters on simulating residual stress in cold spray and will serve as a valuable reference for future studies.

**Keywords** cold spray · finite element analysis · hole drilling method · modeling parameters · residual stress

## Introduction

Cold spray is a solid-state material deposition technology that uses powder particles to create coatings, repair components, or produce near-net-shape additive manufacturing, among other applications (Ref 1-3). The powder particles, which have diameters of 5-50  $\mu\text{m}$ , are accelerated by high-pressure gas to speeds of 500-1200 m/s and impact the substrate at temperatures below the melting point of the sprayed material (Ref 4-6). Albeit being extensively studied, the bonding mechanisms in the cold spray are still under debate and several theories have been proposed, including adiabatic shear instability (Ref 4), mechanical interlocking (Ref 7), mechanical material mixing interlocking (Ref 8), viscous mixing (Ref 9), shockwave effect (Ref 10), amorphization and atomic level intermixing (Ref 11), and so on. Nevertheless, for metallic particles and substrate, it is widely accepted that when the particle speed reaches or exceeds its critical velocity, intense plastic deformation occurs between the particle/substrate and particle/particle interfaces, resulting in adhesion and accumulation (Ref 4, 12). Cold spray's low-temperature

✉ Fanchao Meng  
mengfanchao@ytu.edu.cn

✉ Xin Chu  
xin.chu@hotmail.com

<sup>1</sup> Institute for Advanced Studies in Precision Materials, Yantai University, Yantai 264005, Shandong, China

<sup>2</sup> National Engineering Laboratory for Modern Materials Surface Engineering Technology, Institute of New Materials, Guangdong Academy of Sciences, Guangzhou 510650, Guangdong, China

operation avoids the drawbacks of conventional thermal spray, such as oxidation, undesirable phase transformation, decomposition, chemical reaction, thermally-induced defects, grain growth, and so on (Ref 1, 2). Therefore, the cold spray has garnered intensive research interest for the past 30 years and has been extensively applied in various sectors, such as aerospace (Ref 13, 14), biomedical (Ref 15, 16), energy (Ref 17, 18), electronics (Ref 19, 20) fields.

With the development of cold spray gradually shifting from laboratory research to industrial applications (Ref 1, 2), residual stress in cold spray coatings has become a critical issue as it can induce cracking and delamination in the coatings and compromise the coating integrity, which ultimately affects the performance and service lifetime of the coatings (Ref 21–28). The residual stresses in the cold spray are mainly attributed to peening, quenching, and thermal stresses (Ref 2, 29), but the quenching and thermal stresses were reported to be negligible when the deposition temperature is lower than 400 °C for coating materials and substrates with the same/similar thermo-mechanical properties (Ref 21, 22, 30, 31). Various methods have been used to measure the residual stress in cold spray, such as neutron diffraction (ND) (Ref 21, 25, 32), X-ray diffraction (XRD) (Ref 24, 33–36), in situ curvature measurement (Ref 29), hole drilling (Ref 24), layer removal (Ref 37), focused ion beam ring-core milling (Ref 23, 38), contour method (Ref 32), etc. ND and XRD are the most widely used non-destructive methods for residual stress measurement. For example, Luzin et al. (Ref 21) employed ND to investigate the residual stress profiles in cold-sprayed Cu and Al coatings and observed that the residual stress is tensile near the coating/substrate interface and compressive elsewhere, which is mainly due to kinetic effects rather than thermal effects and depends on the processing parameters and properties of the particle and substrate. However, Boruah et al. (Ref 32) reported that it is the compressive stress that exists near the coating/substrate interface for cold-sprayed Ti-6Al-4V coatings by ND. Ghelichi et al. (Ref 33, 35) applied XRD to measure the residual stress in Al and Al alloy coatings and Al alloy substrate and found that the residual stress is entirely compressive. Another XRD analysis by Matejicek et al. (Ref 36) revealed that the residual stress in cold-sprayed Cu coatings is determined by the properties of the particle and substrate rather than the processing parameters. Therefore, it seems that there are inconsistencies in the results of residual stress in cold spray among experimental studies.

Due to the challenges and limitations in accurately measuring residual stress in cold spray, numerical simulations based on finite element analysis (FEA) have been also extensively used to investigate the distributions of residual stress in cold spray (Ref 22, 23, 26, 27). Among the FEA studies, the Eulerian method that can avoid severe

element distortion and thereby avoid artificial results has gained more and more research interest in modeling cold spray (Ref 39–42). In this context, Li et al. (Ref 22) employed a thermo-mechanical coupled Eulerian model using Abaqus/Explicit to study the influence of particle velocity, temperature, and material combination on the residual stress in Cu coatings on Cu and Al substrates. For the single-pass coating, the authors observed that both compressive and tensile stresses existed in the coating. However, the residual stress profile showed an unusual trend at particle velocities of 600 and 300 m/s for Cu/Cu and Cu/Al material combination, respectively, and the simulated residual stress is different from the ND measurement by Luzin et al. (Ref 21). A later study by Sun et al. (Ref 27) remarked that the mesh size used by Li et al. (Ref 22) was larger than the single particle's deposition, thus being too coarse to obtain realistic results as the Eulerian method was also dependent on the mesh size. These authors thus built a multiple-particle Eulerian model with finer mesh to study the residual stress and found the residual stress is tensile at the interface between the Cu coating and Cu substrate. This hints that the accurate modeling parameters in FEA are essential for analyzing the residual stress and comparing it with the experimental results.

Previously, Li et al. (Ref 43) conducted a comprehensive study on how the modeling parameters affect the impact behaviors of cold spray using Abaqus/Explicit with the Lagrangian formulation. Ghelichi et al. (Ref 33, 35) also discussed various aspects of FEA modeling of residual stresses using the Lagrangian method, such as the impact of particle size and shape, initial velocity, impact angle, post-impact annealing, and processing temperature. However, to the best of the authors' knowledge, there is a lack of detailed information on how the modeling parameters influence the simulation of residual stress in cold spray based on the Eulerian method. Therefore, there is a need for general guidelines for choosing the appropriate modeling parameters to facilitate the modeling of residual stress using this method. Moreover, it remained unclear how and where the stress was extracted from the simulation model. Some previous studies took stress along the axisymmetric line for the 3D single-particle model (e.g., (Ref 23)) or along the face center line for the 3D multiple-particle model (e.g., (Ref 34)). However, many studies did not specify how the stress was extracted (e.g., (Ref 22, 27)). Furthermore, it is known that the microstructure of cold spray coatings is very heterogeneous. It is thus doubtful whether the line stress can adequately represent the actual stress state of the coatings. In addition, the evolution of residual stress to its final state and the interplay between strain/strain rate hardening and thermal softening on the residual stress should be further clarified.

Therefore, this study uses a 2D single-particle Eulerian FEA model to investigate how different modeling parameters affect the residual stress in cold spray. The parameters include mesh size, substrate dimension, material failure, initial temperature, particle velocity, and simulation duration. Cu/Cu is chosen as an example of material combination. The study also examines the residual stress evolutions and distributions from the 2D single-particle simulations, followed by stress distributions from the 3D single- and multiple-particle simulations and hole drilling measurements for thick coatings. “[Computational and Experimental Methods](#)” Section describes the computational methods, “[Results](#)” Section presents the results, “[Discussion](#)” Section discusses the findings, and “[Conclusions](#)” Section concludes the study. The study provides guidance for choosing appropriate modeling parameters for simulating the residual stress in cold spray with the Eulerian FEA model and reveals the characteristics of the residual stress in the cold spray of Cu/Cu particle/substrate combination.

## Computational and Experimental Methods

### Constitutive Models and Material Parameters

Isotropic elasticity and Johnson-Cook plasticity models were employed to describe the elastoplastic behaviors of the particle and substrate during cold spray. The Johnson-Cook model was defined as (Ref 44):

$$\bar{\sigma} = [A + B(\bar{\epsilon}^{pl})^n] \left[ 1 + C \ln \left( \frac{\dot{\bar{\epsilon}}^{pl}}{\dot{\bar{\epsilon}}_0^{pl}} \right) \right] \left[ 1 - \left( \frac{T - T_{ref}}{T_m - T_{ref}} \right)^m \right] \quad (\text{Eq 1})$$

where  $\bar{\sigma}$  is the flow stress;  $A$ ,  $B$ ,  $C$ ,  $m$ , and  $n$  are material constants;  $\bar{\epsilon}^{pl}$  is the equivalent plastic strain (PEEQ),  $\dot{\bar{\epsilon}}^{pl}$  is the equivalent plastic strain rate, and  $\dot{\bar{\epsilon}}_0^{pl}$  is a reference strain rate;  $T_{ref}$  is the reference temperature, i.e., the initial temperature of the particle or substrate before impacting, and  $T_m$  is the melting temperature of the material. The Johnson-Cook model effectively integrates strain hardening, strain rate hardening, and thermal softening, and has been extensively employed to investigate the dynamic impact behaviors in the cold spray (Ref 22, 23, 26, 27, 32, 45–48).

Progressive damage and failure of materials during cold spray can be modeled using the Johnson-Cook dynamic failure model, which is defined as (Ref 49):

$$\bar{\epsilon}_{pf} = \left[ d_1 + d_2 \exp \left( d_3 \frac{p}{q} \right) \right] \left[ 1 + d_4 \ln \left( \frac{\dot{\bar{\epsilon}}^{pl}}{\dot{\bar{\epsilon}}_0^{pl}} \right) \right] \left[ 1 + d_5 \left( \frac{T - T_{ref}}{T_m - T_{ref}} \right)^m \right] \quad (\text{Eq 2})$$

where  $\bar{\epsilon}_{pf}$  is the equivalent plastic strain at material failure;  $\frac{p}{q}$  is the ratio between pressure and deviatoric stress, where  $p$  is the pressure stress and  $q$  is the von Mises stress;  $d_1$ – $d_5$  are failure parameters.

Cu was chosen as the material for both the particle and substrate. The constant and temperature-dependent material properties and Johnson-Cook parameters required for the FEA are shown in Table 1 (Ref 4, 43). Note that for room-temperature (25 °C) deposition, constant material properties were used based on the results of a benchmark study with a particle impact velocity of 600 m/s. The results indicated that the residual stress distributions using constant and temperature-dependent material properties exhibited an insignificant difference (see Supplementary Information Fig. S1 for details). However, for systems with initial temperatures higher than 25 °C, temperature-dependent thermo-mechanical properties were employed as the increased temperature would thermally soften the material, affecting the deposition behavior (Ref 50). The comparisons of residual stresses from constant and temperature-dependent material properties for modeling systems with initial temperatures higher than 25 °C are presented in Supplementary Information Fig. S2.

### FEA Model Set-up

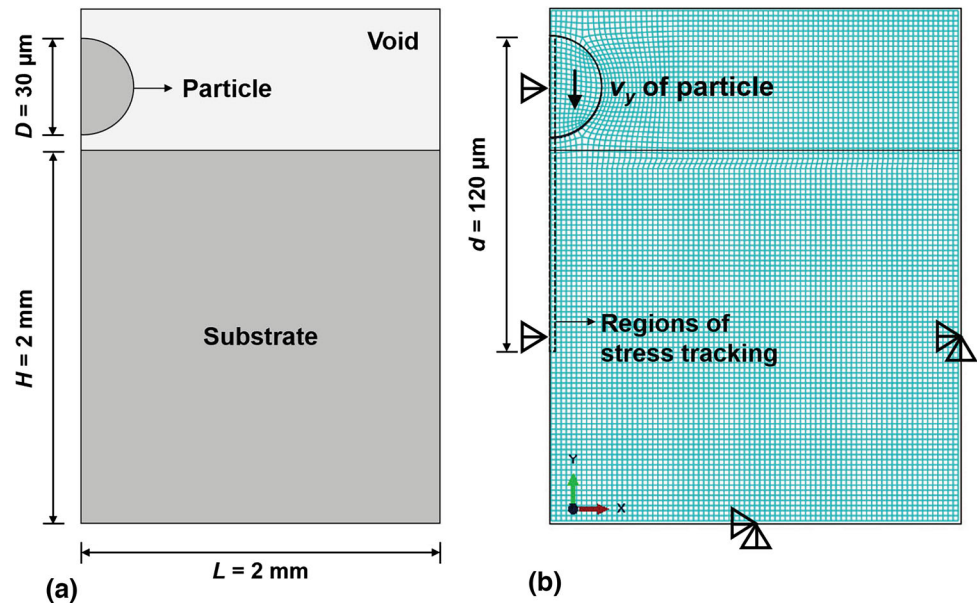
The cold spray process was modeled using Abaqus/Explicit with fully coupled thermal stress analysis. The Eulerian 2D single-, 3D single-, and 3D multiple-particle models were studied. During the Eulerian analysis, the regions of the particle and substrate were filled with materials, while the rest of the space was empty. The mesh remained undeformed and materials flow through the mesh during the impact process. The element type was the 3D 8-node thermally coupled linear Eulerian brick element with reduced integration and hourglass control, EC3D8RT. Note that contact properties between the particle and substrate were not required for the Eulerian model. Previous studies reported that residual stress mainly resulted from the significant plastic deformation of the coating materials for particles and substrates with the same material if the deposition temperature was lower than 400 °C, while the quenching and thermal stresses were negligible (Ref 30). Therefore, the simulation did not consider heat transfer.

For the single-particle model, both 2D and 3D models were employed to examine the residual stresses. The 2D model had only one element in the thickness direction since only 3D elements can be used for Eulerian analysis in Abaqus/Explicit. Nevertheless, the 2D model helps significantly reduce the computational cost, thus serving as a practical model for parametric studies. Other approaches for 2D models are plane strain or axisymmetric

**Table 1** Material properties and parameters for Cu used in the FEA. For the general and elastic properties, both constant (Ref 4) and temperature-dependent (Ref 51) properties were listed. In the Value column,  $T$  represents the temperature

Property	Parameter	Unit	Value	
General	Density	kg/m <sup>3</sup>	8960	8962.77-0.53T
	Specific heat	J/kg K	383	379.9 + 0.1T
	Conductivity	W/m K	386	389.45-3.05 × 10 <sup>-5</sup> T-2.57 × 10 <sup>-5</sup> T <sup>2</sup>
	$T_m$	°C	1083	1083
	Thermal expansion	1/K	5 × 10 <sup>-5</sup>	16.7 × 10 <sup>-6</sup> + 3.74 × 10 <sup>-9</sup> T
	Inelastic heat fraction	...	0.9	0.9
Elastic	Young's modulus	MPa	1.24 × 10 <sup>5</sup>	129.13-0.0668T
	Poisson's ratio	...	0.34	0.34
Plastic	A, B	MPa	90, 292	
	n, m, C	...	0.31, 1.09, 0.025	
	$T_{ref}$	°C	25, 200	
	$\dot{\epsilon}_0^p$	1/s	1	
Damage	$d_1, d_2, d_3, d_4, d_5$	...	0.54, 4.89, - 3.03, 0.014, 1.12	

**Fig. 1** (a) FEA 2D single-particle model set-up and its dimensions. (b) Mesh (the mesh size is for illustration only), boundary conditions, and schematics illustrating the regions where residual stress was tracked. Note that some irregular quadrilateral elements were used to accurately describe the particle shape, the influence of which should be alleviated by a very fine mesh size



formulations. As shown in Fig. 1, the 2D single-particle model was comprised of three parts, a particle with a diameter  $D = 30 \mu\text{m}$ , a square substrate with a height and length of  $H = L = 2 \text{ mm}$ , and an Eulerian body completely enveloping the particle and substrate. Four different mesh sizes were selected that were 0.4, 0.6, 0.8, and 1.0  $\mu\text{m}$  to examine the effect of mesh size on the resultant residual stress. The cold spray impact process was initiated by assigning an initial velocity to the particle. Four initial velocities were considered, being  $v_y = 500, 600, 700,$  and  $800 \text{ m/s}$ , respectively. Moreover, three combinations of particle/substrate initial temperature were considered, which were denoted as  $25 \text{ }^\circ\text{C}/25 \text{ }^\circ\text{C}$ ,  $200 \text{ }^\circ\text{C}/25 \text{ }^\circ\text{C}$ , and  $25 \text{ }^\circ\text{C}/200 \text{ }^\circ\text{C}$ , respectively. Note that at an initial temperature of  $200 \text{ }^\circ\text{C}$ , oxide formation could occur. However, a recent study by Rahmati et al. (Ref 52), who explicitly modeled

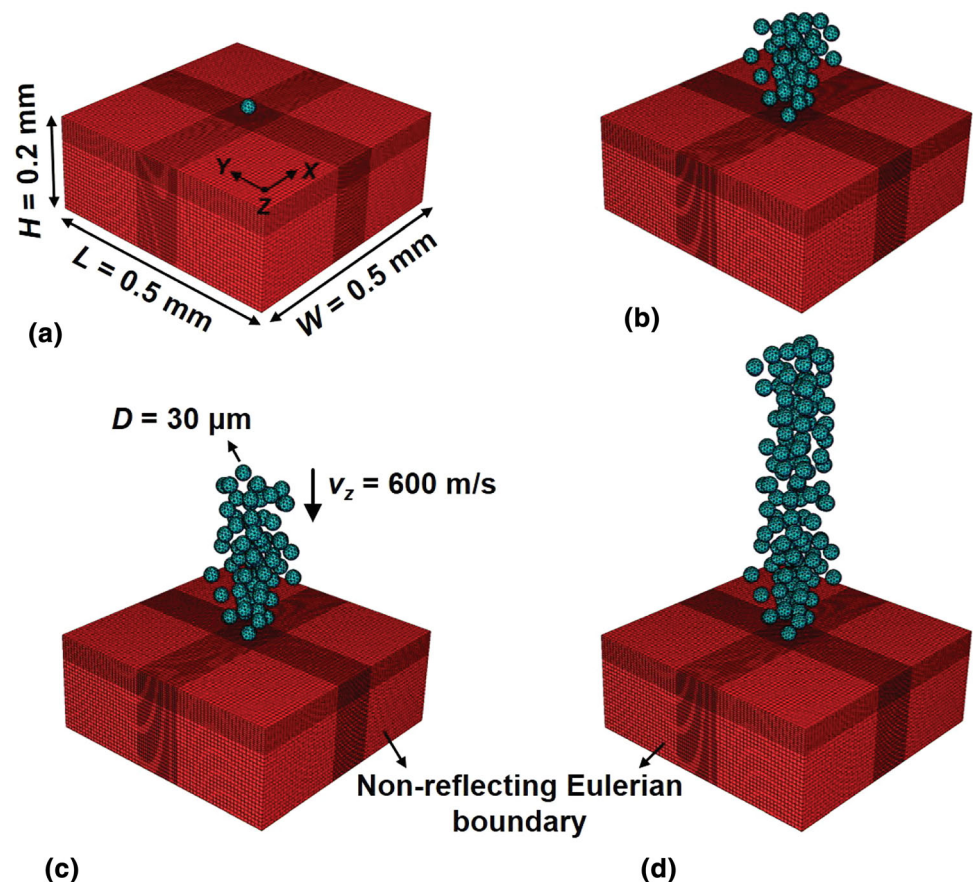
the oxide layer by including its breakage and removal during cold spray impact, demonstrated that the effect of the oxide layer was negligible on the plastic deformation. Therefore, we did not model the oxide layer, assuming that it would not affect the residual stresses. The boundary conditions were applied as follows: (1) constraining the Z direction of the model to approximate the 2D model; (2) constraining the X and Y directions of the bottom and right surfaces; and (3) constraining the X direction of the left surfaces (see Fig. 1b). After impacting, the residual stress along the Y direction, i.e.,  $\sigma_{yy}$  (out-of-plane stress), was extracted from the through-thickness elements along the axisymmetric axis from the top surface of the particle into a depth of  $d = 120 \mu\text{m}$ , as shown in Fig. 1(b). Note that the out-of-plane stress was also extracted for analysis by some previous studies (Ref 22, 27, 53). Stress tracking was

performed on impact time points of 50, 100, 200, and 1000 ns to analyze the evolutions and distributions of the residual stress. It is worth noting that the tracked regions covered the entire particle and part of the substrate along the axis of symmetry after the impact.

Figure 2(a), (b), (c) and (d) illustrate the 3D single- and multiple-particle models, respectively, in which the particles were placed on the top surface of the substrate, and the multiple particles were created randomly by using a random seed. The distance between adjacent particles is around 20–50  $\mu\text{m}$ , which means that a particle with a speed of 500 m/s would take about 40–100 ns to travel. As the kinetic energy of a single particle *completely* dissipates in  $\sim 200$  ns (see Fig. 8), the distance between impacting particles is shorter than the time required for a single particle to finish its deposition ( $\sim 200$  ns), i.e., the next particle will collide with a depositing particle upon impact. This scenario is in agreement with many other cold spray studies, where multiple particles were modeled (Ref 27, 54). Moreover, due to the strong interference of factors such as supersonic gas flow in different directions above the substrate, it is very hard to experimentally determine the distance between impacting particles and to give an accurate value. However, from an experimental point of view, a very similar condition is suggested by literature

(Ref 55, 56) that the subsequent particles will collide with an impacting particle before it completely deposits. Thus, the model is expected to match the experiment and provide reliable residual stress calculation. All particles' diameters were 30  $\mu\text{m}$ . The length, width, and height of the substrate were 0.5, 0.5, and 0.2 mm, respectively. To avoid artificial stresses resulting from the substrate boundaries, non-reflecting Eulerian boundary conditions were applied to the side and bottom surfaces of the substrate to model a semi-infinite substrate. The initial temperature of the particle(s) and substrate in all the 3D single- and multiple-particle models was 25  $^{\circ}\text{C}$ . The 3D single-particle model investigated the effect of impact velocities from 500 to 800 m/s on residual stresses. While the 3D multiple-particle model examined the evolution of residual stress with the coating thickness. In the 3D multiple-particle model, the number of particles simulated was 43, 70, and 128, and the initial velocity of all the particles was 600 m/s, which was close to the experimental particle velocity (see Section “[Experimental Measurement of Residual Stress](#)” for details). The Eulerian mesh size enclosing and underneath the particles' region was 1.5  $\mu\text{m}$ , and elsewhere was 3  $\mu\text{m}$ . Due to the computational limitations, a finer mesh than 1.5  $\mu\text{m}$  was not used for the 3D models. Nevertheless, as shown in Supplementary Information Fig. S3, a

**Fig. 2** 3D single- and multiple-particle FEA models with the number of particles being (a) one, (b) 43, (c) 70, and (d) 128. Non-reflecting Eulerian boundary conditions were imposed on the side and bottom surfaces of the substrate. The mesh is only for illustration



comparison of residual stresses using the 3D single-particle model with an initial velocity of 600 m/s showed negligible differences.

Due to the highly heterogeneous distributions of the residual stresses in the coatings, 6 cross sectional planes were sliced out along the height direction, and within each slice three representative regions were tracked to extract the residual stresses (see Supplementary Information Fig. S4-S11 for details). Subsequently, the multi-slice multi-track averaged stresses were calculated for analysis. To differentiate the  $\sigma_{yy}$  (out-of-plane stress) in Fig. 1, the in-plane stresses  $\sigma_{xx}$  and  $\sigma_{yy}$  were denoted as  $\sigma_{11}$  and  $\sigma_{22}$  and extracted to compare with the in-plane residual stresses measured from the hole drilling method. Based on the kinetic energy evolution of the simulation system with simulation time, the time needed for the 43, 70, and 128 particles to dissipate all the kinetic energy is 360, 640, and 750 ns, respectively. Supplementary Information Fig. S12 provided the kinetic energy evolution of the model with 128 particles. However, the simulation was running for an extended time of 2000 ns to guarantee that the residual stress is in the final state.

Due to practical difficulties, the FEA modeling was not directly validated with experimental measurements of residual stress for the same coating thickness. However, the FEA code, constitutive model, and thermo-mechanical properties of Cu that were used in this study were chosen based on previous experimental validations from different perspectives (Ref 22, 39, 42, 57). Moreover, the boundary conditions were consistent with many other studies (Ref 22, 39, 42, 54). Therefore, it is assumed that the above model is reliable and applicable. It is also known that the flow stresses of some materials have substantial strain rate sensitivity, exhibiting an abrupt rise of the flow stress when a critical strain rate is reached (Ref 58, 59), which theoretically cannot be accurately predicted by the Johnson-Cook model. To address the problem, devoted studies have been reported on developing modified Johnson-Cook models or new constitutive models (Ref 58, 60–66). Nevertheless, the Johnson-Cook model and its parameters for Cu have shown generally good agreement between cold spray experiments and FEA in previous studies (Ref 4, 67). Therefore, the Johnson-Cook model was adopted in this study. Furthermore, this study did not account for the interface bonding as the Eulerian method leads to a sticky interface/perfect bonding. For more information on the effect of interface bonding on residual stresses, the readers can refer to Lin et al.'s study (Ref 31). The study revealed that the interface bonding generally reduced the compressive stress caused by peening, but this effect was limited to the interface region and had little impact on the stress distributions away from the contact interface.

## Experimental Measurement of Residual Stress

The in-plane (i.e., the plane normal to the coating thickness direction) residual stresses of Cu coatings/substrate along the through-thickness direction were measured by the hole drilling method. A prism-type laser keyhole residual stress analyzer by Stresstech Ltd., Finland, was used for the measurement. This analyzer is based on the electronic speckle pattern interferometry (ESPI) method, which detects the displacement by illuminating the region of interest with coherent laser light and analyzing the movement of a speckle pattern. As the surface displacement correlates with the reference beam, displacement information can be obtained by comparing pixels between the surface and its neighbor. The drilling tool tip had a diameter of 3.175 mm and a feed rate of 0.005 mm/s. The first measurement point was at the center of the coating surface and 8 more points were measured underneath it with an even drilling step of 0.1 mm. The total drilling depth was 0.8 mm, which covered both the coatings and substrate. Before drilling and when the drilling reached the target depth, the tool was withdrawn to perform laser displacement analysis. Based on the measured displacement, the software is available to calculate the residual stresses. The mathematical method behind the software had been detailed in the study by Schajer and Steinzig (Ref 68). The values of Young's modulus and Poisson's ratio used for the calculation were 110 GPa and 0.37, respectively (different from the corresponding modeling parameters to some degree as the material parameters used in the modeling were well validated and the present study did not aim to quantitatively compare the magnitude of the residual stress between the two approaches as the coating thickness was different).

The Cu coatings were deposited on the Cu substrate by cold spray using a Plasma Giken PCS-1000 system. The Cu powder was supplied by the Institute of New Materials, Guangdong Academy of Science (# Cu-001). It had a spherical shape with d10, d50, and d90 of 8.3  $\mu\text{m}$ , 23.1  $\mu\text{m}$ , and 51.3  $\mu\text{m}$ , respectively. The SEM image and size distributions of the Cu powders before cold spray are presented in Fig. 3(a) and (b). The substrate surfaces were cleaned with acetone before spraying to remove contaminations. The Cu substrate surface was protected by a plastic film to prevent oxidation. No other surface treatments were applied to avoid process-induced residual stress. The nozzle was a tungsten carbide nozzle with a throat diameter of 2.8 mm, an outlet diameter of 10 mm, and an expansion section length of 20 cm. The robot speed was 300 mm/s and the step size was 1 mm. The feeding rate was 200 g/min. The propulsive gas was nitrogen and the inlet pressure and temperature were 5 MPa and 700 °C, respectively. The coating thickness was 0.7 mm and the

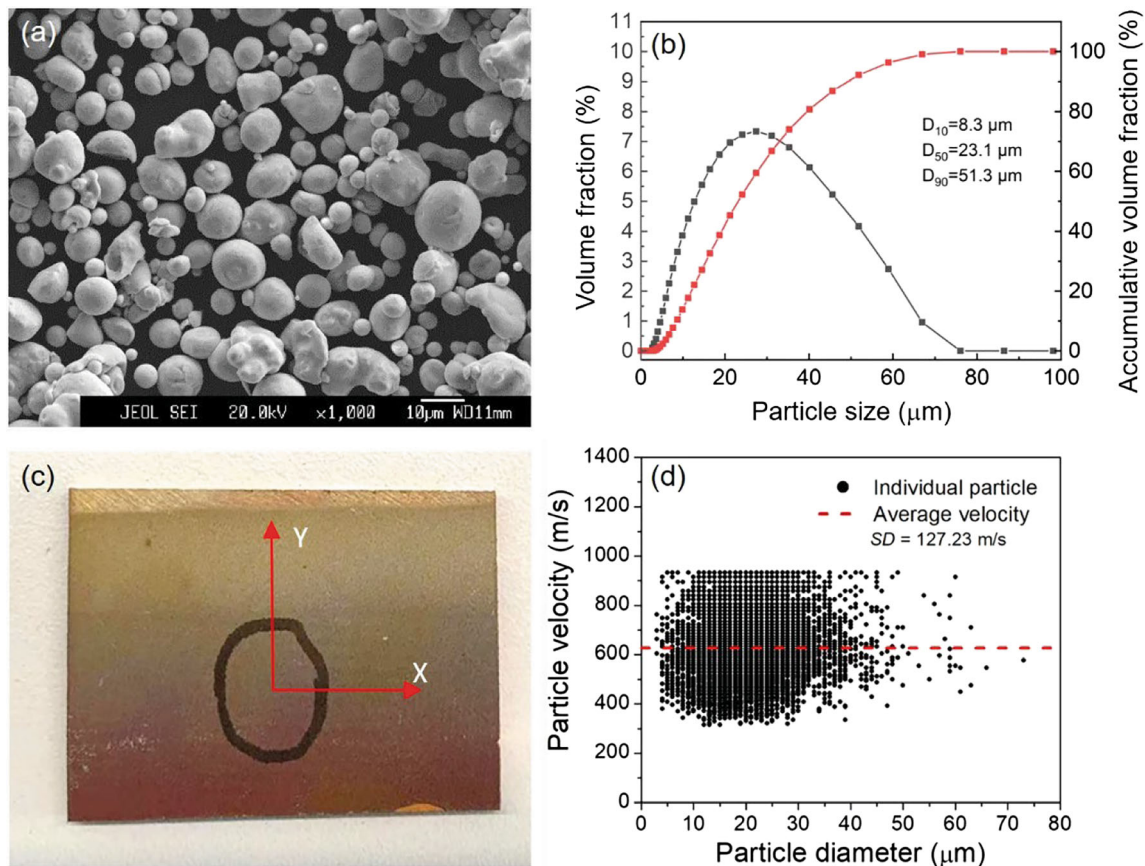


**Fig. 3** (a) Morphologies and (b) size distributions of the Cu powders before cold spray. (c) The cold-sprayed Cu and the measuring position of the residual stress. (d) Experimentally measured particle velocity

specimen for residual stress measurement and the test position are shown in Fig. 3(c). The average particle velocity was calculated based on the particle velocity measurement of 10000 powders using the Tecnar particle diagnostic system DPV-2000, which was 625.78 m/s, as shown in Fig 3(d). The particle velocity in the 3D multiple-particle models was set to be 600 m/s to maintain consistency across the manuscript.

## Results

### Residual Stresses from the 2D Single-particle Simulations

In this section, the effects of mesh size, material failure, and initial temperature on residual stress evolution are investigated by the 2D, one-element thick model described above. The results presented here demonstrate the effects of these parameters and the evolution of stress in general, but they could be limited due to the modeling assumption.

### *The Effects of Mesh Size and Substrate Dimension on Residual Stress*

Figure 4(a) shows the variation in residual stress  $\sigma_{yy}$  to the through-depth thickness  $d$  for different mesh sizes. The particle velocity and initial temperature of the particle/substrate were fixed at  $v_y = 800 \text{ m/s}$  and  $25 \text{ }^\circ\text{C}/25 \text{ }^\circ\text{C}$ , respectively. The substrate size was set as  $H = L = 2 \text{ mm}$ . Figure 4(a) indicates that the value of  $\sigma_{yy}$  and its distribution are affected by the mesh size. Particularly, comparing the residual stresses between coarse (1.0 and 0.8  $\mu\text{m}$ ) and fine (0.6 and 0.4  $\mu\text{m}$ ) mesh sizes, coarse mesh sizes not only underestimate the peak tensile stress but also cause large stress deviation for  $d > 60 \mu\text{m}$ , as shown by the black arrows in Fig. 4(a). Nevertheless, when the mesh size reduces from 0.6 to 0.4  $\mu\text{m}$ , the characteristics of the residual stress distributions show negligible differences. Therefore, a mesh size of 0.6  $\mu\text{m}$  can be considered a convergent solution. This is consistent with Assadi et al.'s study (Ref 4), where an appropriate mesh size was 1/50 of the particle's diameter, i.e., 0.6  $\mu\text{m}$  for  $D = 30 \mu\text{m}$ . Hence, a mesh size of 0.6  $\mu\text{m}$  was adopted for all the following simulations.

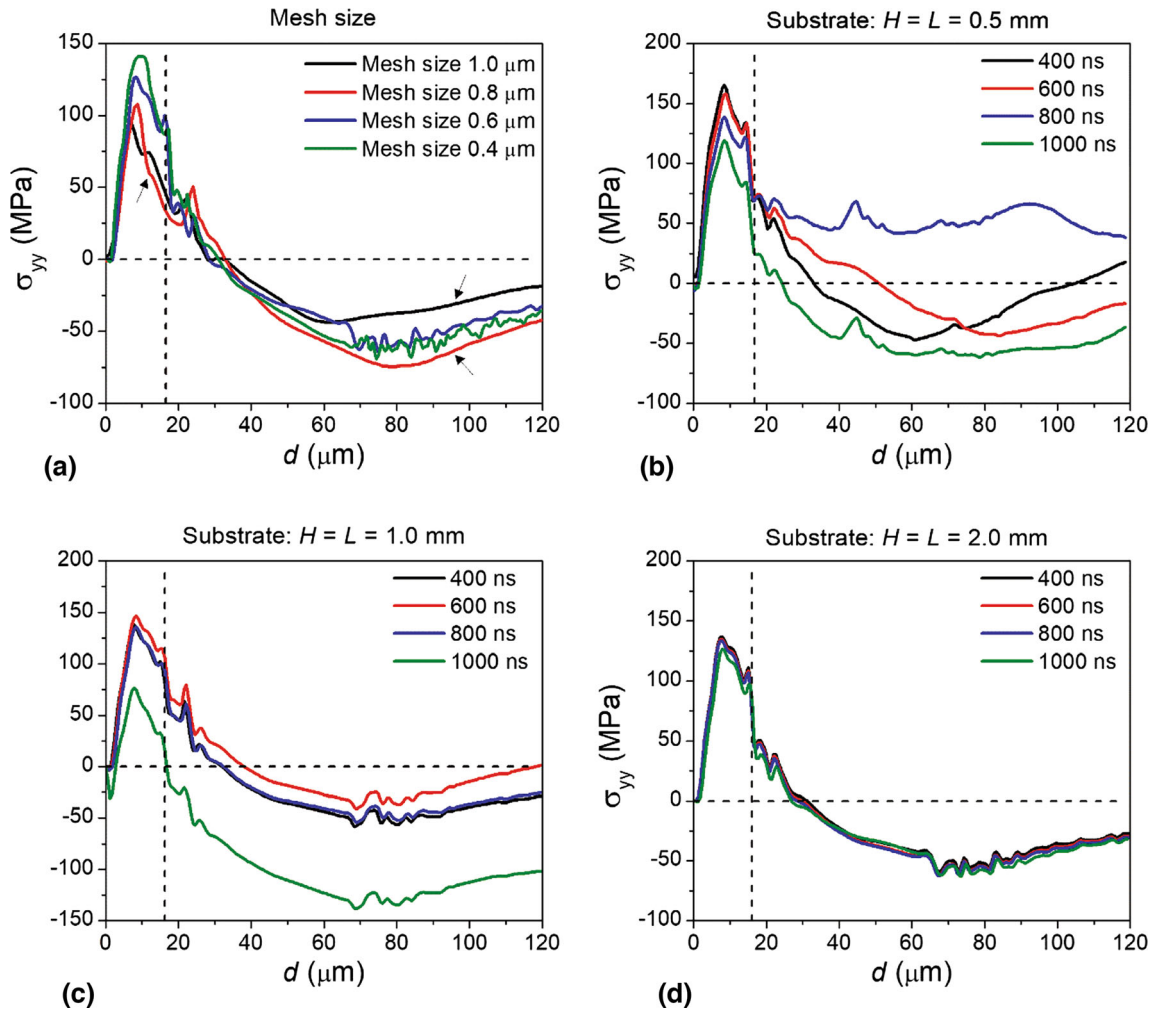


**Fig. 4** The distributions of residual stress  $\sigma_{yy}$  as a function of the through-depth thickness  $d$  under different (a) mesh sizes for a simulation duration of 1000 ns and (b-d) substrate sizes. The horizontal and vertical dash lines indicate the positions of zero residual stress to guide the eye and the position where the

particle/substrate interface locates, respectively. For clarity, one vertical dash line is used for each subfigure as there are no essential differences in the locations of the interfaces among the tested conditions

Figure 4(b), (c) and (d) shows the distributions of  $\sigma_{yy}$  as a function of  $d$  for substrate with dimensions being  $H = L = 0.5, 1,$  and  $2$  mm, respectively, under different simulation durations. The initial conditions for velocity and temperature were the same as those used for the mesh size analysis. Looking at Fig. 4(b), (c) and (d), it is obvious that the distributions of  $\sigma_{yy}$  exhibit huge distinctions among simulation durations from 400 to 1000 ns, and cannot reach stable convergence even for 1000 ns. While for Fig. 4(d), the  $\sigma_{yy}$  distributions are almost identical for all the simulation durations considered, indicating that it is not affected by the simulation duration. Nevertheless, a sufficiently long simulation duration, such as 1000 ns, is suggested for the accuracy of the stress simulation. Therefore, choosing an appropriate substrate dimension is crucial for obtaining reliable results of the residual stress using the Eulerian

formulation. It is worth noting that previous studies often used substrate dimensions of  $H = L = 1$  mm for a particle with  $D = 30 \mu\text{m}$  (Ref 4, 45-47). However, our study found that this size was not adequate for the convergence of the residual stress based on the Eulerian formulation. The following results in this study were therefore obtained using a substrate size of  $H = L = 2$  mm and a simulation duration of 1000 ns.

To understand the reasons underlying the stress fluctuations concerning simulation durations in Fig. 4(b), we analyzed the deformed configurations of the particle and substrate with  $\sigma_{yy}$  contours for substrate sizes with  $H = L = 0.5$  mm. We observed that inadequate sizes of the substrate will cause stress to bounce at the boundaries, thus significantly altering the simulated stress distributions (see more details in Supplementary Information Fig. S13).

### The Effects of Material Failure on Residual Stress

The residual stress  $\sigma_{yy}$  along the through-depth thickness  $d$  before and after accounting for the material failure under different particle velocities are shown in Fig. 5. The particle and substrate had an initial temperature of 25 °C. By comparison, the stress distributions are similar for both cases whether including material failure. This is because the failure of the material mainly occurs around the jetting region, while the stress tracking regions are located far from the jetting. To verify if the material failure has any effect on the residual stress distributions, we have tracked the stress inside and below the jetting region. We have found that the stress distributions are not affected by the material failure even in the jetting region (see Supplementary Information S14 for details). Therefore, material failure has been ignored in the subsequent analysis of the paper.

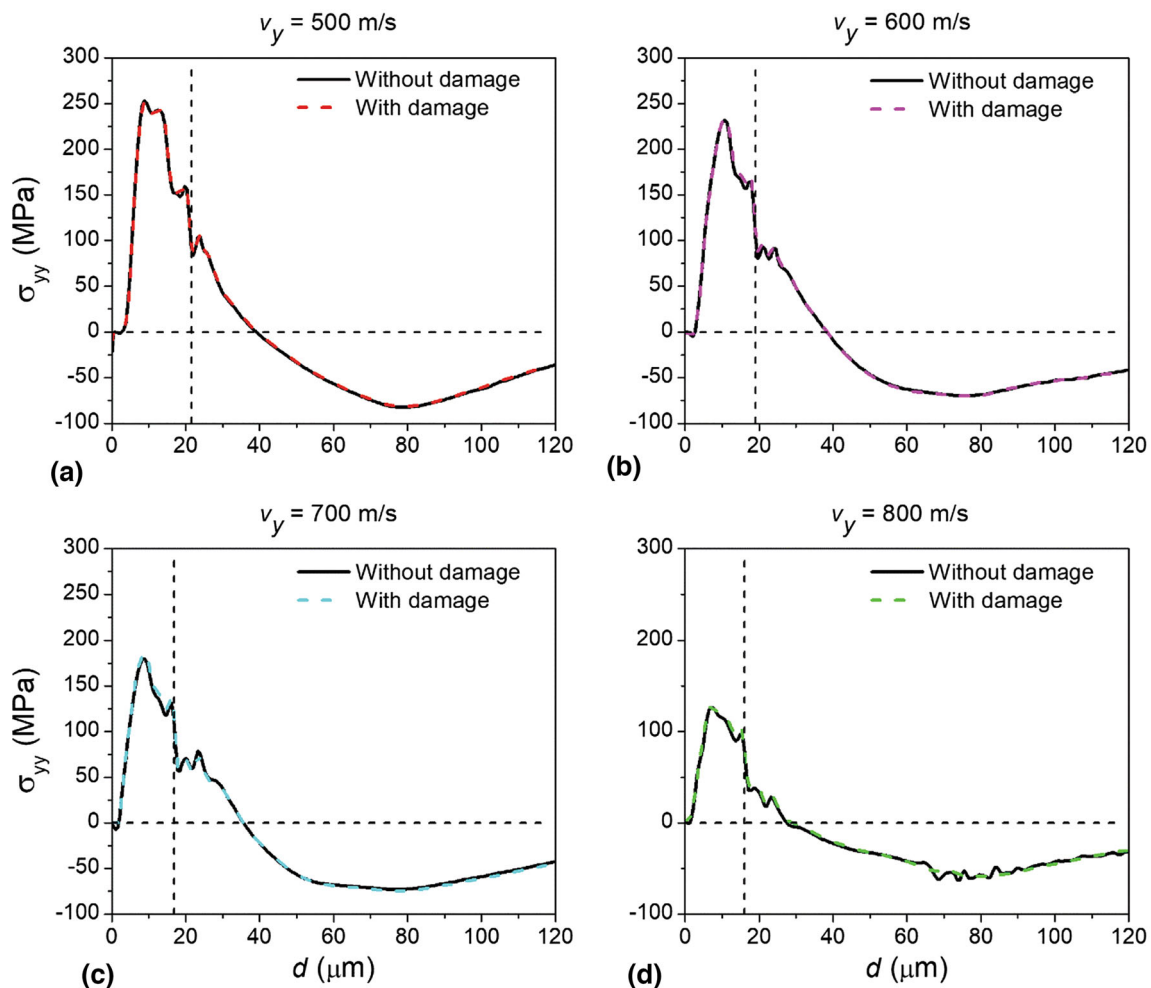


**Fig. 5** The distributions of residual stress  $\sigma_{yy}$  from the 2D model as a function of the through-depth thickness  $d$  for materials with and without failure under particle velocities of (a) 500 m/s, (b) 600 m/s,

### The Effects of Initial Temperature on Residual Stress

Figure 6 shows how  $\sigma_{yy}$  varies along the through-depth thickness  $d$  for three groups of initial temperatures of the 2D single-particle/substrate under different particle velocities. It can be seen that the overall trends of the residual stresses are similar for different initial temperatures, and they can be described by three stages: (1) a rapid increase in tensile stress from the initial value to a maximum; (2) a decrease in tensile stress until it becomes negative and reaches a minimum compressive stress; and (3) a gradual reduction of the compressive stress magnitude. Furthermore, owing to the thermal softening effect, the residual tensile and compressive stresses both decrease when the initial temperature increases from 25 to 200 °C. The above observations remain valid for particle velocities in the range of 500–800 m/s.

It is further observed that the effect of initial temperature on the stress distribution is more pronounced at lower

(c) 700 m/s, and (d) 800 m/s, respectively. The horizontal and vertical dash lines indicate the zero stress and particle/substrate interface, respectively

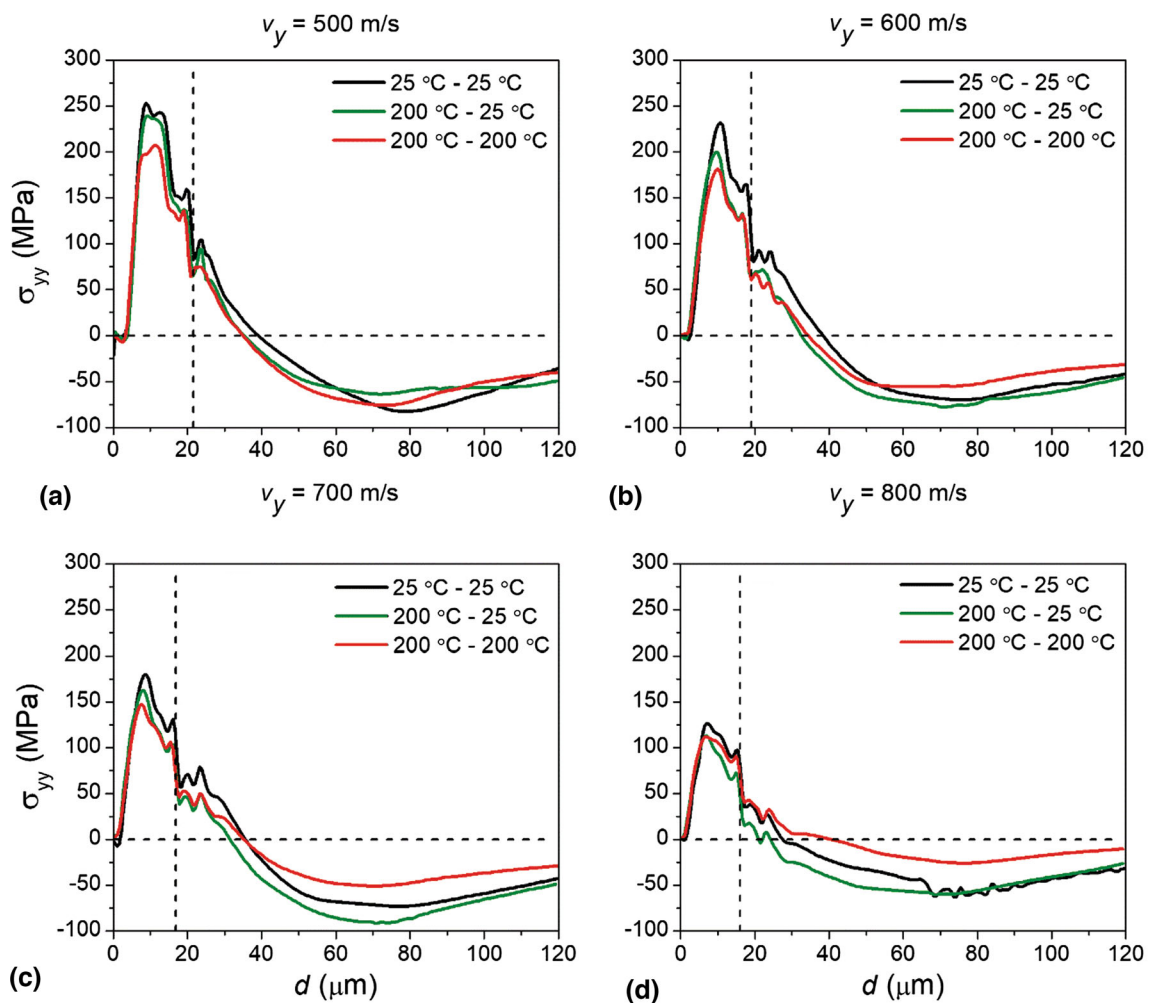


**Fig. 6** The distributions of residual stress  $\sigma_{yy}$  as a function of the through-depth thickness  $d$  for the three groups of initial material temperatures under particle velocities of (a) 500 m/s, (b) 600 m/s, (c) 700 m/s, and (d) 800 m/s, respectively. The horizontal and vertical

dash lines indicate the zero stress and particle/substrate interface, respectively. For clarity, one vertical dash line is used for each subfigure as the locations of the interfaces among the tested conditions are nearly the same

particle velocities. By defining the “maximum stress difference” as the absolute value of the largest difference in stress among the three temperature groups at the same depth. For  $v_y = 500, 600, 700,$  and  $800$  m/s, the maximum stress differences are 76.02, 71.48, 44.81, and 43.84 MPa, respectively. This is because, at lower velocities, the increase in the initial temperature of the material dominates the thermal softening behavior over the temperature rise caused by plastic deformation. Consequently, the increase in initial temperature shows more evident effects on stress reduction when the velocity is lower.

Furthermore, the values of the through-depth thickness  $d$  corresponding to the maximum stress differences are 14.25, 18.46, 9.46, and 46.05  $\mu\text{m}$ , respectively, for particle velocities from 500 to 800 m/s. Therefore, the maximum stress differences are within the particle for  $v_y = 500\text{--}700$  m/s and within the substrate for  $v_y = 800$  m/s. This is because the heat generated by plastic deformation around

the impact zone is higher than the initial temperature when the particle velocity is high. Therefore, for the impact zone, the increase in initial temperature from 25 to 200  $^{\circ}\text{C}$  is less important when particle velocity is as high as 800 m/s. However, for  $v_y = 800$  m/s, the initial temperature is mainly reflected in the interior of the substrate. Therefore, the initial temperature has a larger impact on the particle stress for low velocities and on the substrate stress for high velocities.

*The Distributions and Evolutions of Residual Stress*

To thoroughly analyze the distributions of the residual stress, Fig. 7 plots  $\sigma_{yy}$  as a function of  $d$  under different particle velocities with the initial temperature of the particle/substrate being 25  $^{\circ}\text{C}/25$   $^{\circ}\text{C}$  and simulation duration being 1000 ns. A comparison of  $\sigma_{yy}$  among different

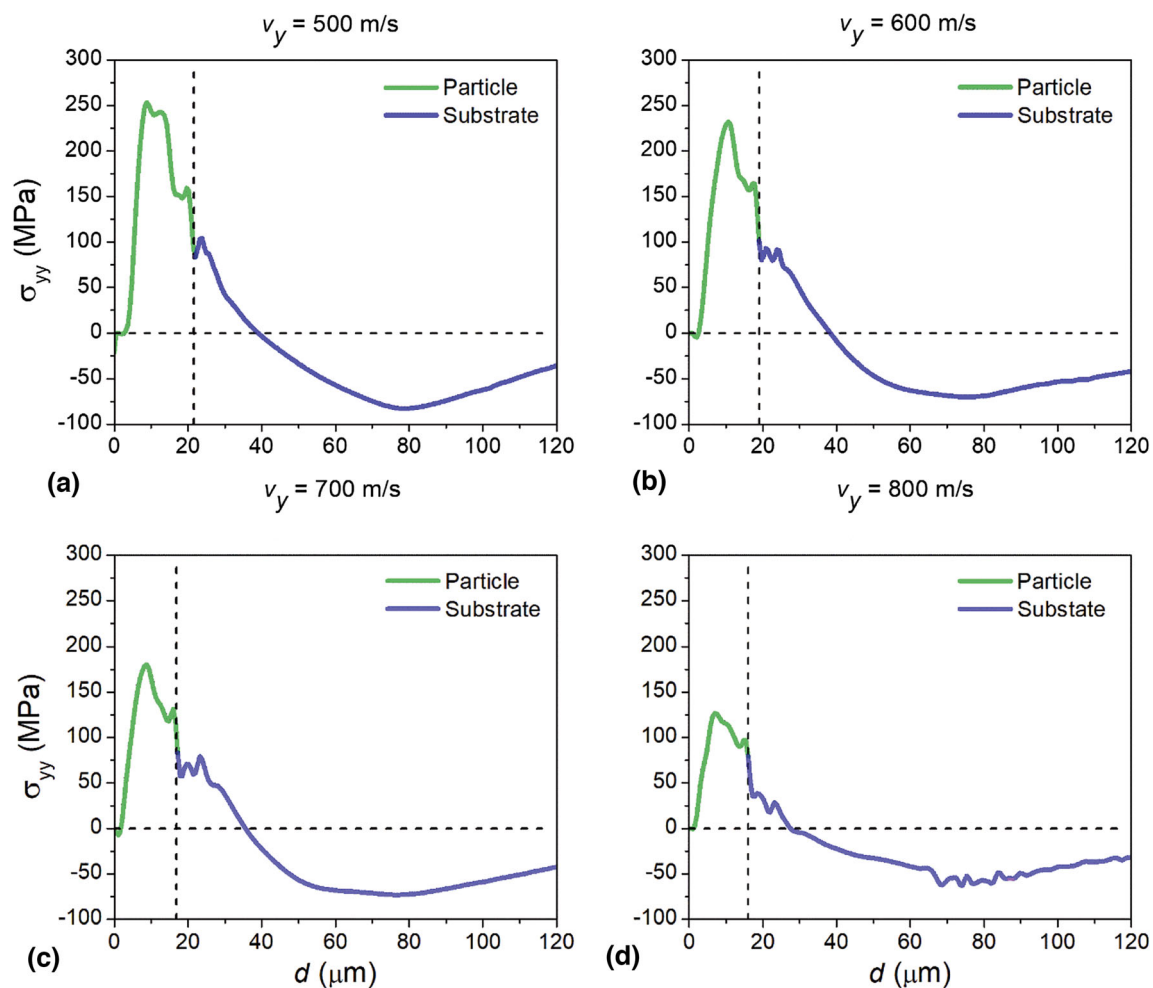


**Fig. 7** The distributions of residual stress  $\sigma_{yy}$  as a function of the through-depth thickness  $d$  for initial particle/substrate temperatures being 25 °C/25 °C under particle velocities of (a) 500 m/s, (b) 600 m/s

s, (c) 700 m/s, and (d) 800 m/s, respectively. The horizontal and vertical dash lines indicate the zero stress and particle/substrate interface, respectively

velocities reveals that the stress variations are compressive-tensile-compressive from the surface of the particle down into the substrate, and that the impact velocity is inversely proportional to the absolute values of the tensile and compressive stresses. Specifically, for  $v_y = 500, 600, 700,$  and  $800$  m/s, the maximum tensile stress is 253.59, 232.11, 180.03, and 126.37 MPa, respectively, and the maximum compressive stress is  $-82.77, -70.17, -73.18,$  and  $-62.72$  MPa, respectively. As analyzed in Section “[The Effects of Initial Temperature on Residual Stress](#)”, lower velocities generate lower levels of thermal softening, thus resulting in larger residual stress.

Further analysis reveals that at  $d \leq 1\text{--}3 \mu\text{m}$ , the particle surface and near-surface are under compressive stress. With the increase in  $d$ , the residual stress switches from compression to tension and increases quickly. The highest tensile stress is near the center of the deformed particle. Subsequently, the tensile stress drops fast as  $d$  increases and there is tensile stress at the particle/substrate interface,

which agrees with Li et al.’s studies (Ref 22, 69). They suggested that the friction shear of the interfacial layers and their interactions caused the tensile residual stress. The stress at the particle/substrate interface is around 55, 69, 59, and 35 MPa, respectively, corresponding to the impact velocity in the range of 500–800 m/s. Moreover, tensile stress is present at the substrate surface and 8–14  $\mu\text{m}$  below it for different velocities. With further increase in  $d$  into the substrate, tensile stress becomes compressive stress, which keeps rising until it starts to decrease gently at  $d = 70\text{--}80 \mu\text{m}$ . It is noteworthy that quenching-induced tensile stress might affect the final stress profile, but its effect on the stress magnitude is likely small, particularly for Cu, which has high density and medium-high coefficient of thermal expansion (CTE) (Ref 29).

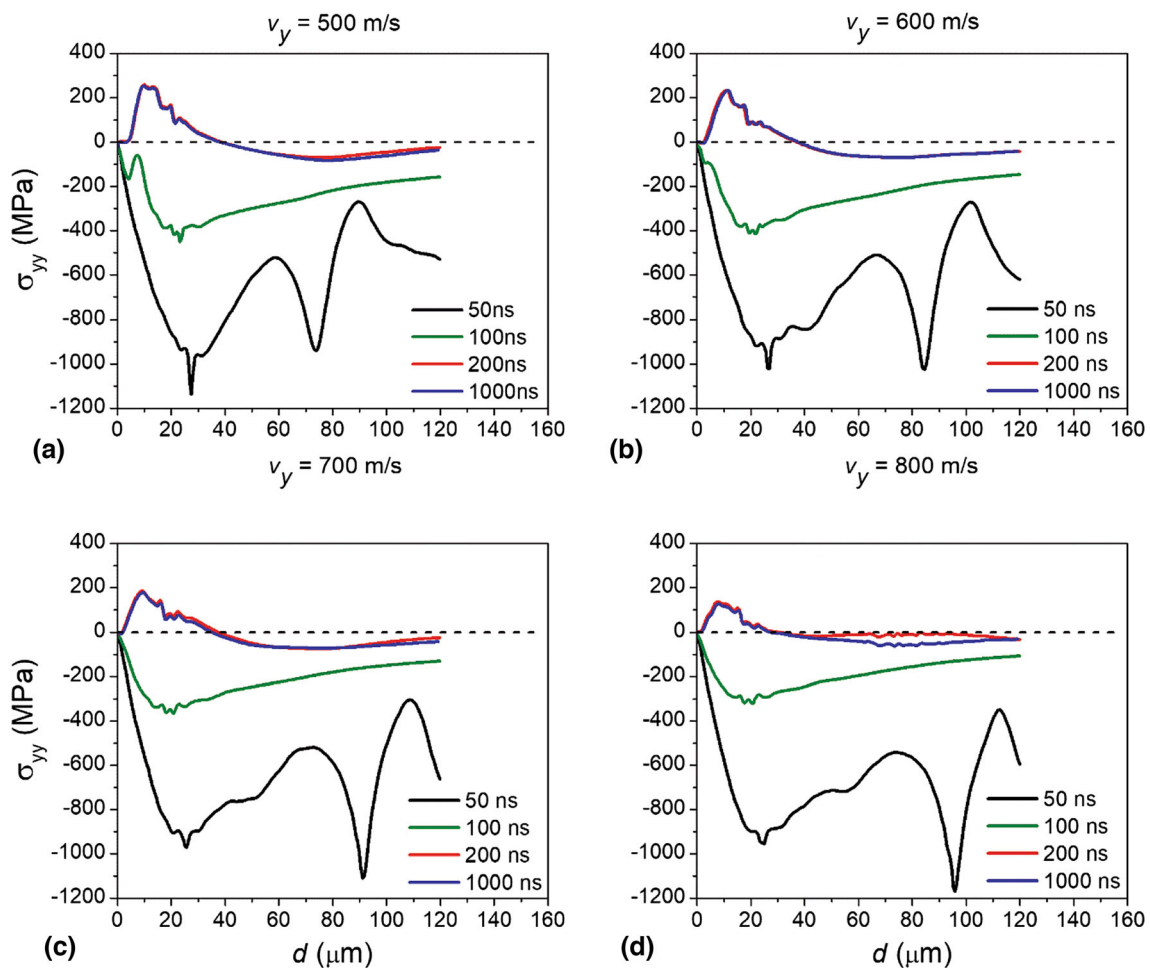
The results shown in Fig. 7 have a similar trend to those obtained by Luzin et al. (Ref 21), who used the ND method to investigate the residual stress distribution of cold-sprayed Cu coatings on Cu substrate. Moreover, unlike Li

et al.’s study (Ref 22), where stress distributions at 600 m/s are anomalous compared with those of 300, 500, and 700 m/s for Cu/Cu material combination, the present study reveals a monotonic trend in the stress distribution with increasing particle velocity.

To study the evolutions of the residual stress during impact, Fig. 8 plots the distributions of residual stress at 50, 100, 200, and 1000 ns, respectively, under different particle velocities for initial particle/substrate temperatures being 25 °C/25 °C. The results show that at 50 ns, the residual stresses are compressive in both the particle and substrate and the stresses in the substrate vary greatly with  $d$  for all the particle velocities considered. At 100 ns, the residual stresses of the particle and substrate decrease significantly, but they remain compressive and the highest compressive stresses are near the particle–substrate interface. At 200 ns, the stress distributions are similar to those at 1000 ns, which have been discussed in detail in Section “The Distributions and Evolutions of Residual

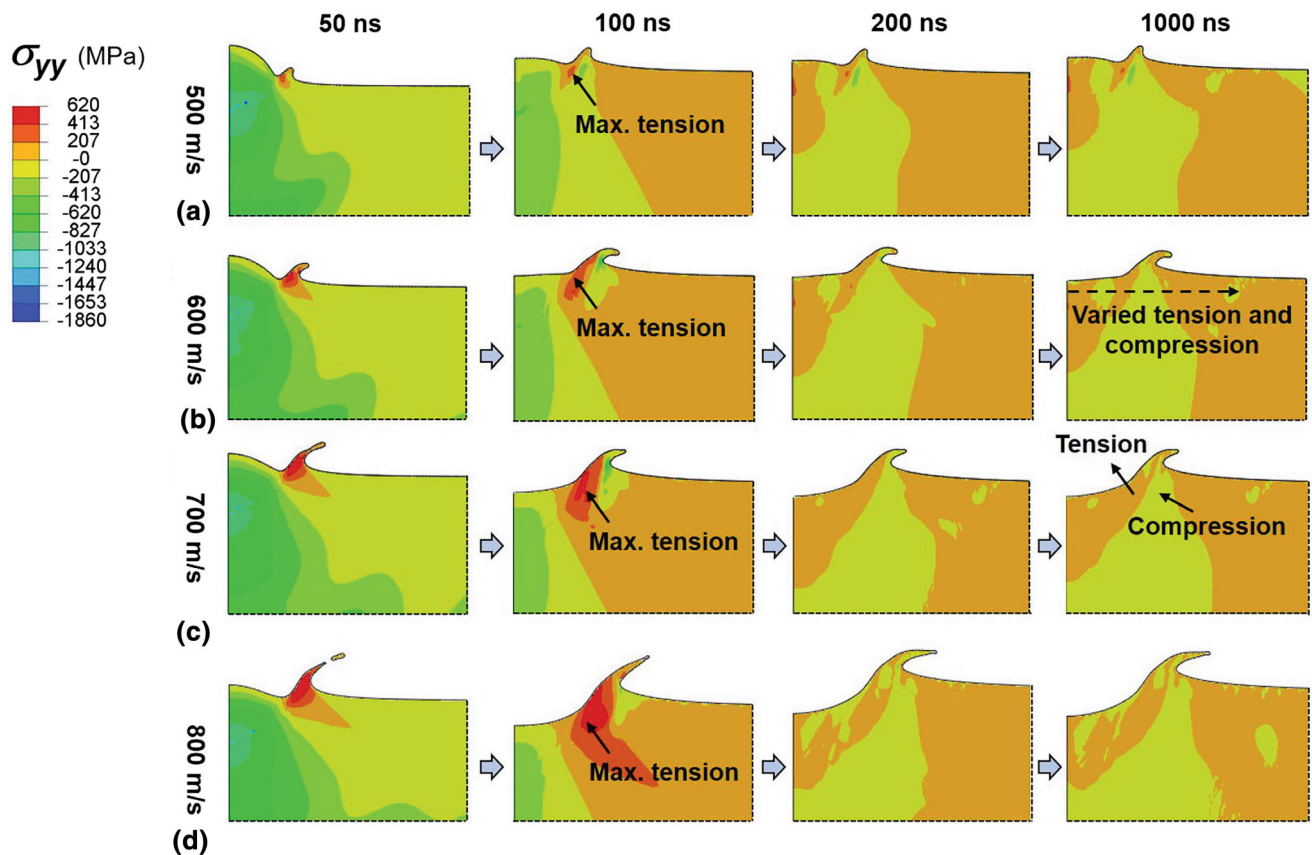
Stress”. This indicates that the stress distributions converge after 200 ns of simulation time, which is consistent with some previous studies (Ref 4, 45–47).

Figure 9 shows the deformed configurations of the 2D single-particle/substrate with the residual stress  $\sigma_{yy}$  contours at different time steps during the 1000 ns simulation duration under different particle velocities. The results indicate that material jetting emerges at 50 ns for all the particle velocities considered, and its extent increases with the simulation time, as evidenced by the increased flattening ratio of the particle. Moreover, at the same time point, higher impact velocity induces higher degrees of flattening ratio to the particle. Furthermore, at 50 and 100 ns, residual stresses are compressive for both the particle and the substrate within the stress tracking regions. Afterward, at 200 ns, the residual stresses evolve from compressive stress into the coexistence of tensile and compressive stresses, and remain nearly unchanged until 1000 ns (see Fig. 9c). The maximum tensile stresses are



**Fig. 8** The distributions of residual stress  $\sigma_{yy}$  as a function of the through-depth thickness  $d$  at different time points during the 1000 ns simulation duration under particle velocities of (a) 500 m/s,

(b) 600 m/s, (c) 700 m/s, and (d) 800 m/s, respectively. Four simulation time points, being 50, 100, 200, and 1000 ns, were selected



**Fig. 9** The deformed configurations of the particle/substrate with contours of residual stress  $\sigma_{yy}$  at different time points during the 1000 ns simulation duration under particle velocities of (a) 500 m/s,

(b) 600 m/s, (c) 700 m/s, and (d) 800 m/s, respectively. Four simulation time points, being 50, 100, 200, and 1000 ns, were selected

located near the left side of the material jetting and both tensile and compressive stresses coexist within the jetting zone, which may lead to interface cracking, in agreement with Li et al. (Ref 22). Additionally, Fig. 9(b) shows that the residual stress along the horizontal direction varies in its sign, which is also consistent with Li et al.'s study (Ref 22).

### Residual Stresses from the 3D Single-particle Simulations

The averaged residual stresses from the 6 slices of each model (see Supplementary Information Fig. S5–S8 for details) concerning impact velocity for the 3D single-particle simulations are shown in Fig. 10. The simulation duration is 2000 ns and initial temperatures of the particle and substrate are 25 °C. To make a direct comparison of the residual stresses of the 3D single-particle (i.e., in-plane stresses) with those of the 2D single-particle model. The in-plane stress ( $\sigma_{xx}$ ) from the 2D single-particle model was extracted and shown in Fig. S15. The results show that the simulated  $\sigma_{11}$  and  $\sigma_{22}$  overlap with each other, which is consistent with previous experimental results that the in-

plane stress is biaxial within experimental uncertainties (Ref 70). This conclusion is also confirmed by our hole drilling experiments as shown in Fig. 11(d). The residual stress distributions and magnitudes to the through-depth thickness  $d$  from the 3D single-particle simulation have similar trends with that of 2D single-particle simulation, except that the interface stress of the 2D simulation changes from being tensile to compressive with the increase in impact velocity (Fig. 10 versus Fig. S15). This difference can be explained by the difference in the extraction regions of the residual stresses. For the 3D single-particle model, the regions were extracted to calculate averaged residual stresses of the whole deformed particle and the substrate underneath it. For the 2D single-particle model, the residual stresses were extracted along the axisymmetric axis of the particle down into the substrate, i.e., regions around the south pole of the particle, where the deformation is less severe than the peripheral regions, e.g., around the jetting. From the deformed configurations at 1000 ns of the 2D single-particle simulations in Fig. 9, the distribution of the residual stresses is heterogeneous and depends on the location. The heterogeneity of the stresses is also seen in the 3D single-particle simulations, as shown in Fig. S4 of

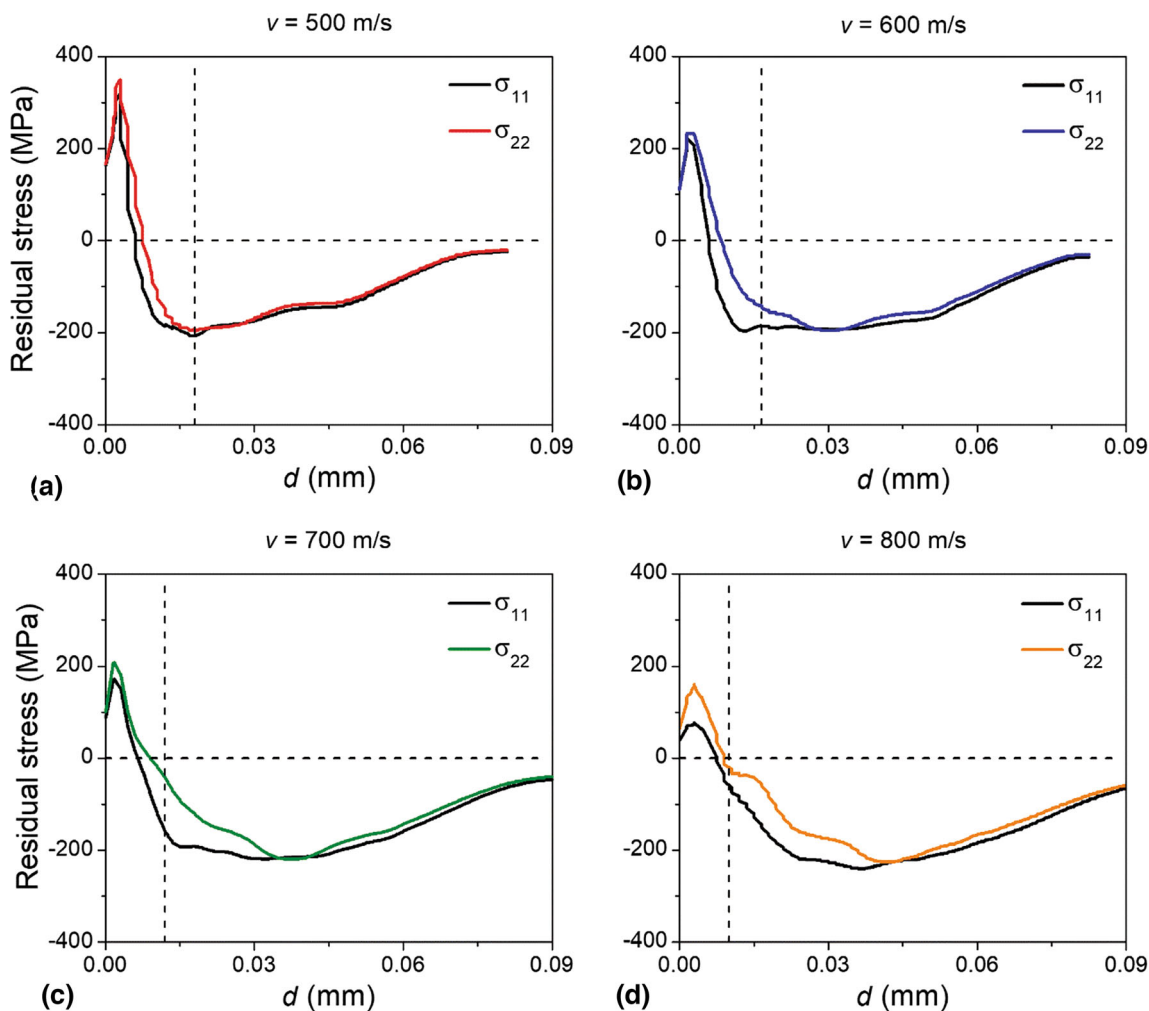


**Fig. 10** Residual stresses from the 3D single-particle simulations as a function of the through-depth thickness  $d$  for particle velocities in (a) 500 m/s, (b) 600 m/s, (c) 700 m/s, and (d) 800 m/s. The horizontal

and vertical dash lines represent the zero stress and the coating/substrate interface, respectively

the Supplementary Information. Moreover, the residual stresses decrease in magnitude as the particle velocity increases, which is consistent with the 2D single-particle simulations. This behavior can be explained by the thermal softening effect that becomes more pronounced as the particle velocity increases, as discussed in Section “The Effects of Initial Temperature on Residual Stress”.

### Residual Stresses from the 3D Multiple-particle Simulations and Experiment

The multi-slice multi-track averaged residual stresses (see Supplementary Information S4 and S9-S11 for details) for the 3D multiple-particle simulations are shown in Fig. 11(a) and (c), and experimentally measured ones are shown in Fig. 11(d). The residual stress distribution from 43 particles simulation is similar to that of 3D single-particle simulation. The residual stresses along the through-

depth direction are compressive for all simulations with different numbers of particles from 43 to 70 and 128, which matches the experimental results. This is because of the extensive and successive kinetic impact of the particles. Fig. 11(b), (c) and (d) shows that with the increase in  $d$ , the compressive residual stresses first increase, and then decrease when approaching the substrate, which is in good agreement with the literature for Cu splats/coatings (Ref 21, 36). Fig. 11(c) and (d) show that the simulated residual stress is higher than the experimental one. This may be because the interface bonding was not modeled in the study. Another reason may be that the experimental coating thickness (0.7 mm, Fig. 11d) is one order of magnitude larger than that of the simulation (0.08 mm, Fig. 11c). As it is computationally difficult to simulate such a thick coating. We examine how the simulated residual stresses evolve with the number of particles, i.e., the coating thickness. It is interesting to see that the residual stresses

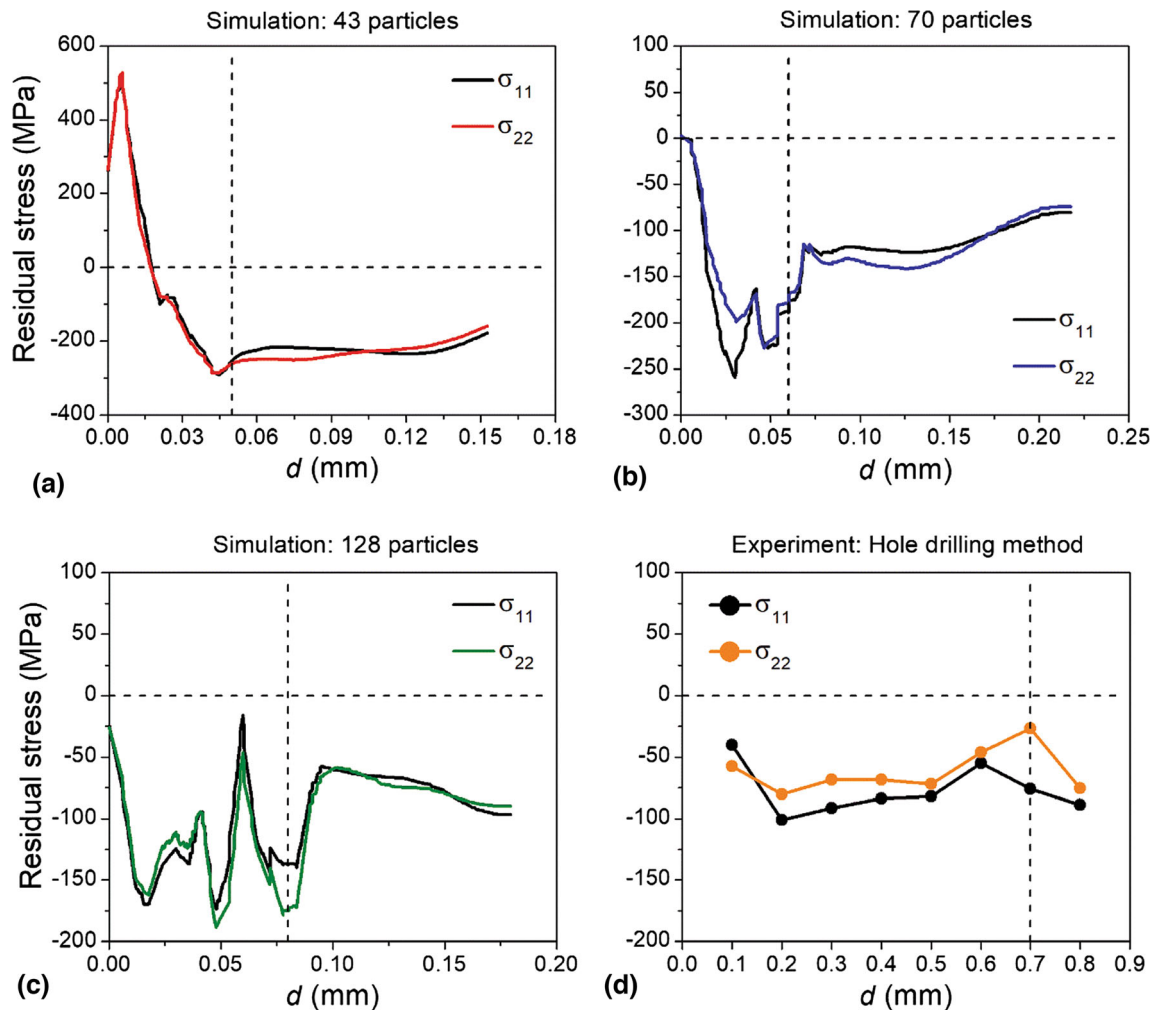


**Fig. 11** Residual stresses from multiple-particle simulations in (a) 43 particles, (b) 70 particles, and (c) 128 particles, and from (d) experiment measured using hole drilling method as a function of the

through-depth thickness  $d$ . The horizontal and vertical dash lines represent the zero stress and the coating/substrate interface, respectively

decrease with the coating thickness, which suggests that thermal softening reduces the residual stress as the coating layers are building up. Therefore, even though the current simulation cannot simulate the experimental coating thickness, it could be reasonably speculated that the magnitude of the residual stress could approach those from the experiment with increasing simulated particles. The Supplementary Information Fig. S16 shows the 3D multiple-particle simulations with  $\sigma_{11}$  contours, which illustrate the deformed configurations of the coatings.

## Discussion

From the results of 2D single-particle (Fig. 6 and S15), 3D single-particle (Fig. 10), and 3D multiple-particle (Fig. 11) models, it is unveiled that the residual stresses are mainly deposition/peening stresses that result from the impact-

induced deformation of the particle(s) and substrate. Wherein, thermal softening due to the increase in initial temperature and/or plastic deformation-induced temperature rise has a significant effect on reducing the residual stresses. To quantify the effect of thermal softening, the thermal softening term, i.e., the third bracket in Eq 1, is excluded to re-simulate the residual stresses using the 2D single-particle model with an initial temperature of 25 °C. Comparisons of the results tracked along the axisymmetric axis of the particle with those including thermal softening are presented in Fig. 12. It is seen that including thermal softening mainly reduces the residual stresses within the substrate for each velocity and its effect is more noticeable for higher velocities, which have more deformation-induced temperature rises. Note that Hassani-Gangaraj et al. (Ref 10) used the FEA Lagrangian method and found that including or excluding thermal softening in the Johnson-Cook model has little influence on the strain distribution

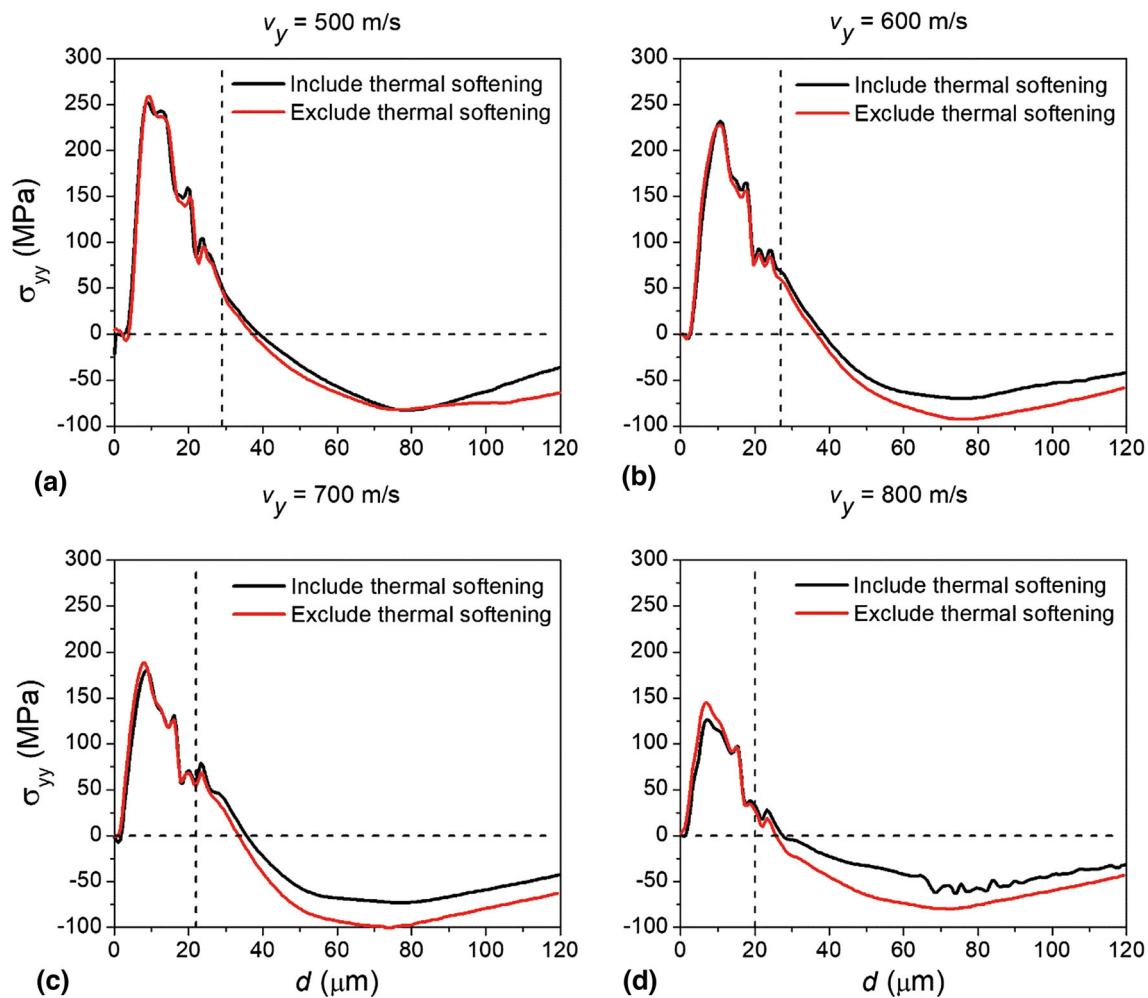


**Fig. 12** Comparisons of residual stresses as a function of the through-depth thickness  $d$  between including and excluding thermal softening effect in the Johnson-Cook model using the 2D single-particle model

with particle velocities of (a) 500 m/s, (b) 600 m/s, (c) 700 m/s, and (d) 800 m/s, respectively. The horizontal and vertical dash lines indicate the zero stress and particle/substrate interface, respectively

and particle flattening, but could affect material deformation and failure around the jetting region, where thermal softening contributes mostly to the deformation. As the stress we tracked is away from the jetting, it is seen that the stress in the particle from Fig. 12 changes slightly whether including thermal softening, which is generally consistent with the reference finding (Ref 10). For more details on the relationship between temperature evolution and residual stress development during the actual cold spray process, we refer to a system-level study by Lin et al. (Ref 71).

### Conclusions

In summary, based on a Cu/Cu 2D single-particle/substrate Eulerian finite element model, we clarified how different modeling parameters, such as mesh size, substrate dimension, material failure, initial temperature, particle velocity,

and simulation duration, influenced the accuracy of the simulated residual stress distributions in cold spray. The results show that the mesh size, substrate dimension, and simulation duration have significant effects on the residual stress distributions. For the Cu/Cu combination with a particle diameter of 30  $\mu\text{m}$ , these parameters are suggested to be 0.6  $\mu\text{m}$ , 2 mm  $\times$  2 mm, and 200 ns, respectively. While the material failure has negligible effects because it localizes within the jetting region. Moreover, an increase in the initial temperature of the material decreases the residual stress due to thermal softening, and its effect is more evident when the particle velocity is lower because plastic deformation-induced heat dominates the thermal softening over the initial temperature at higher velocities. Based on these modeling parameters, the evolutions and distributions of the residual stress along the axisymmetric line of the particle are analyzed. The residual stress evolves from initially being compressive to finally becoming

compressive-tensile-compressive from the particle surface to the substrate with tensile interfacial stress caused by friction shear. Furthermore, the multi-slice multi-track averaged stress was taken to account for the stress heterogeneity when analyzing the 3D simulations. The 3D single-particle simulations show generally similar residual stress distributions and variations concerning impact velocity with the 2D simulations. Finally, the 3D multiple-particle simulations follow a similar trend to those from hole drilling measurements, exhibiting compressive stresses within the coatings and substrate, and the plastic deformation-induced thermal softening mechanisms underlying the decrease in residual stresses with the increase in coating thickness are clarified. The present study formulates guidelines on the selection of Eulerian-based FEA modeling parameters to simulate residual stress in cold spray and clarifies the residual stress evolution and the effect of thermal softening on residual stress, which shall be valuable for future experimental and FEA studies.

**Supplementary Information** The online version contains supplementary material available at <https://doi.org/10.1007/s11666-023-01640-z>.

**Acknowledgment** Fanchao Meng acknowledges financial support from the Natural Science Foundation of Shandong Province (ZR2021QE110). Xin Chu is grateful for financial support from the Guangdong Academy of Sciences Special Fund for Comprehensive Industrial Technology Innovation Center Building (2022GDASZH-2022010107) and Guangdong Basic and Applied Basic Research Foundation (2021A1515110326).

## References

1. E. Irissou, D. Poirier, P. Vo, C.V. Cojocar, M. Aghasibeig, and S. Yue, How to Unleash the Remarkable Potential of Cold Spray: A Perspective, *J. Therm. Spray Technol.*, 2022, **31**(4), p 908-919.
2. W. Sun, X. Chu, H. Lan, R. Huang, J. Huang, Y. Xie, J. Huang, and G. Huang, Current Implementation Status of Cold Spray Technology: A Short Review, *J. Therm. Spray Technol.*, 2022, **31**, p 1-18.
3. A. Alkhimov, V. Kosarev, and A. Papyrin, A Method of Cold Gas-Dynamic Spraying, *Dokl. Akad. Nauk SSSR*, 1990, **315**(5), p 1062-1065.
4. H. Assadi, F. Gärtner, T. Stoltenhoff, and H. Kreye, Bonding Mechanism in Cold Gas Spraying, *Acta Mater.*, 2003, **51**(15), p 4379-4394.
5. R. Dykhuizen and M. Smith, Gas Dynamic Principles of Cold Spray, *J. Therm. Spray Technol.*, 1998, **7**(2), p 205-212.
6. R. Dykhuizen, M. Smith, D. Gilmore, R. Neiser, X. Jiang, and S. Sampath, Impact of High Velocity Cold Spray Particles, *J. Therm. Spray Technol.*, 1999, **8**(4), p 559-564.
7. T. Hussain, D. McCartney, P.H. Shipway, and D. Zhang, Bonding Mechanisms in Cold Spraying: The Contributions of Metallurgical and Mechanical Components, *J. Therm. Spray Technol.*, 2009, **18**(3), p 364-379.
8. M. Grujicic, J.R. Saylor, D.E. Beasley, W. DeRosset, and D. Helfritsch, Computational Analysis of the Interfacial Bonding between Feed-Powder Particles and the Substrate in the Cold-Gas Dynamic-Spray Process, *Appl. Surf. Sci.*, 2003, **219**(3-4), p 211-227.
9. V.K. Champagne, D. Helfritsch, P. Leyman, S. Grendahl, and B. Klotz, Interface Material Mixing Formed by the Deposition of Copper on Aluminum by Means of the Cold Spray Process, *J. Therm. Spray Technol.*, 2005, **14**(3), p 330-334.
10. M. Hassani-Gangaraj, D. Veysset, V.K. Champagne, K.A. Nelson, and C.A. Schuh, Adiabatic Shear Instability is not Necessary for Adhesion in Cold Spray, *Acta Mater.*, 2018, **158**, p 430-439.
11. K. Ko, J. Choi, and H. Lee, The Interfacial Restructuring to Amorphous: A New Adhesion Mechanism of Cold-Sprayed Coatings, *Mater. Lett.*, 2016, **175**, p 13-15.
12. M. Grujicic, C.L. Zhao, W.S. DeRosset, and D. Helfritsch, Adiabatic Shear Instability Based Mechanism for Particles/Substrate Bonding in the Cold-Gas Dynamic-Spray Process, *Mater. Des.*, 2004, **25**(8), p 681-688.
13. V.K. Champagne Jr., O.C. Ozdemir, and A. Nardi, *Practical Cold Spray*, Springer, Cham, 2021.
14. V. Champagne and D. Helfritsch, Critical Assessment 11: Structural Repairs by Cold Spray, *Mater. Sci. Technol.*, 2015, **31**(6), p 627-634.
15. A. Moridi, E.J. Stewart, A. Wakai, H. Assadi, F. Gartner, M. Guagliano, T. Klassen, and M. Dao, Solid-State Additive Manufacturing of Porous Ti-6AL-4V by Supersonic Impact, *Appl. Mater. Today*, 2020, **21**, p 100865.
16. X. Chu, R. Chakrabarty, H. Che, L. Shang, P. Vo, J. Song, and S. Yue, Investigation of the Feedstock Deposition Behavior in a Cold Sprayed 316L/Fe Composite Coating, *Surf. Coat. Technol.*, 2018, **337**, p 53-62.
17. J. Tam, W. Li, B. Yu, D. Poirier, J.-G. Legoux, P. Lin, G. Palumbo, J.D. Giallonardo, and U. Erb, Reducing Complex Microstructural Heterogeneity in Electrodeposited and Cold Sprayed Copper Coating Junctions, *Surf. Coat. Tech.*, 2020, **404**, p 126479.
18. H. Yeom and K. Sridharan, Recent Advances of Cold Spray Technology in Nuclear Energy Applications, *J. Adv. Mater. Process.*, 2020, **178**(5), p 61-63.
19. A. Vardelle, C. Moreau, J. Akedo, H. Ashrafizadeh, C.C. Berndt, J.O. Berghaus, M. Boulos, J. Brogan, A.C. Bourtsalas, and A. Dolatabadi, The 2016 Thermal Spray Roadmap, *J. Therm. Spray Technol.*, 2016, **25**(8), p 1376-1440.
20. V. Kosarev, S. Klinkov, B. Melamed, Y.K. Nepochatov, N. Ryashin, and V. Shikalov, Cold Spraying for Power Electronics: Deposition of Thick Topologically Patterned Copper Layers on Ceramics, in AIP Conference Proceedings, AIP Publishing LLC, 2018, p 030047.
21. V. Luzin, K. Spencer, and M.-X. Zhang, Residual Stress and Thermo-Mechanical Properties of Cold Spray Metal Coatings, *Acta Mater.*, 2011, **59**(3), p 1259-1270.
22. W. Li, K. Yang, D. Zhang, and X. Zhou, Residual Stress Analysis of Cold-Sprayed Copper Coatings by Numerical Simulation, *J. Therm. Spray Technol.*, 2016, **25**(1), p 131-142.
23. X. Song, J. Everaerts, W. Zhai, H. Zheng, A.W.Y. Tan, W. Sun, F. Li, I. Marinescu, E. Liu, and A.M. Korsunsky, Residual Stresses in Single Particle Splat of Metal Cold Spray Process—Numerical Simulation and Direct Measurement, *Mater. Lett.*, 2018, **230**, p 152-156.
24. K. Bobzin, W. Wietheger, M. Knoch, A. Schacht, U. Reisgen, R. Sharma, and L. Oster, Comparison of Residual Stress Measurements Conducted by X-Ray Stress Analysis and Incremental Hole Drilling Method, *J. Therm. Spray Technol.*, 2020, **29**(6), p 1218-1228.
25. R. Sinclair-Adamson, V. Luzin, A. Duguid, K. Kannoorpatti, and R. Murray, Residual Stress Distributions in Cold-Sprayed Copper 3d-Printed Parts, *J. Therm. Spray Technol.*, 2020, **29**(6), p 1525-1537.

26. A. Faheem, A. Tyagi, F. Hasan, A.A. Khan, Q. Murtaza, K.K. Saxena, Residual Stress Investigation in the Metallic Coating Approach of Micro-Sized Particles on the Substrate: Cold Spray Additive Manufacturing, *Adv. Mater. Process. Technol.*, 2022, p 1-17.
27. C. Sun, W. Gui, J. Lu, L. Xie, and Y. Wu, Comparison of the Deposition Process for Metallic and Mg Coatings Using Cold Spraying, *J. Therm. Spray Technol.*, 2022, **31**, p 1155-1172.
28. B. Marzbanrad, E. Toyserkani, and H. Jahed, Fatigue Crack Initiation in Cold Spray Coated Az31b-H24 with Aa7075 Powder, *Int. J. Fatigue*, 2022, **163**, p 107084.
29. T. Suhonen, T. Varis, S. Dosta, M. Torrell, and J. Guilemany, Residual Stress Development in Cold Sprayed Al, Cu and Ti Coatings, *Acta Mater.*, 2013, **61**(17), p 6329-6337.
30. A.S.M. Ang and C.C. Berndt, A Review of Testing Methods for Thermal Spray Coatings, *Int. Mater. Rev.*, 2014, **59**(4), p 179-223.
31. E. Lin, Q. Chen, O.C. Ozdemir, V.K. Champagne, and S. Müftü, Effects of Interface Bonding on the Residual Stresses in Cold-Sprayed Al-6061: A Numerical Investigation, *J. Therm. Spray Technol.*, 2019, **28**(3), p 472-483.
32. D. Boruah, B. Ahmad, T.L. Lee, S. Kabra, A.K. Syed, P. McNutt, M. Doré, and X. Zhang, Evaluation of Residual Stresses Induced by Cold Spraying of Ti-6Al-4V on Ti-6Al-4V Substrates, *Surf. Coat. Tech.*, 2019, **374**, p 591-602.
33. R. Ghelichi, S. Bagherifard, D. MacDonald, I. Fernandez-Pariente, B. Jodoin, and M. Guagliano, Experimental and Numerical Study of Residual Stress Evolution in Cold Spray Coating, *Appl. Surf. Sci.*, 2014, **288**, p 26-33.
34. G. Shayegan, H. Mahmoudi, R. Ghelichi, J. Villafuerte, J. Wang, M. Guagliano, and H. Jahed, Residual Stress Induced by Cold Spray Coating of Magnesium AZ31B Extrusion, *Mater. Des.*, 2014, **60**, p 72-84.
35. R. Ghelichi, D. MacDonald, S. Bagherifard, H. Jahed, M. Guagliano, and B. Jodoin, Microstructure and Fatigue Behavior of Cold Spray Coated Al5052, *Acta Mater.*, 2012, **60**(19), p 6555-6561.
36. J. Matejcek and S. Sampath, Intrinsic Residual Stresses in Single Splats Produced by Thermal Spray Processes, *Acta Mater.*, 2001, **49**(11), p 1993-1999.
37. S. Rech, A. Trentin, S. Vezzù, J.-G. Legoux, E. Irissou, and M. Guagliano, Influence of Pre-Heated Al 6061 Substrate Temperature on the Residual Stresses of Multipass Al Coatings Deposited by Cold Spray, *J. Therm. Spray Technol.*, 2011, **20**(1), p 243-251.
38. N.M. Dang, W.-Y. Lin, Z.-Y. Wang, S.A. Alidokht, R.R. Chromik, T.Y.-F. Chen, and M.-T. Lin, Mechanical Properties and Residual Stress Measurement of Tin/Ti Duplex Coating Using Hipims Tin on Cold Spray Ti, *Coatings*, 2022, **12**(6), p 759.
39. W. Li, K. Yang, S. Yin, and X. Guo, Numerical Analysis of Cold Spray Particles Impacting Behavior by the Eulerian Method: A Review, *J. Therm. Spray Technol.*, 2016, **25**(8), p 1441-1460.
40. C. Sun, X. Zhou, C. Xie, and B. Liu, Investigating Hard/Soft Combinations of Cold Spraying by Eulerian Approach, *Surf. Eng.*, 2020, **36**(10), p 1049-1057.
41. M. Yu, W.-Y. Li, F. Wang, and H. Liao, Finite Element Simulation of Impacting Behavior of Particles in Cold Spraying by Eulerian Approach, *J. Therm. Spray Technol.*, 2012, **21**(3), p 745-752.
42. F. Wang, W. Li, M. Yu, and H. Liao, Prediction of Critical Velocity During Cold Spraying Based on a Coupled Thermo-mechanical Eulerian Model, *J. Therm. Spray Technol.*, 2014, **23**(1), p 60-67.
43. W.-Y. Li, C. Zhang, C.-J. Li, and H. Liao, Modeling Aspects of High Velocity Impact of Particles in Cold Spraying by Explicit Finite Element Analysis, *J. Therm. Spray Technol.*, 2009, **18**(5-6), p 921-933.
44. G.R. Johnson and W.H. Cook, A Constitutive Model and Data for Metals Subjected to Large Strains, High Strain Rates and High Temperatures, in Proceedings of the 7th International Symposium on Ballistics, The Netherlands, 1983, p 541-547.
45. F. Meng, H. Aydin, S. Yue, and J. Song, The Effects of Contact Conditions on the Onset of Shear Instability in Cold-Spray, *J. Therm. Spray Technol.*, 2015, **24**(4), p 711-719.
46. F. Meng, D. Hu, Y. Gao, S. Yue, and J. Song, Cold-Spray Bonding Mechanisms and Deposition Efficiency Prediction for Particle/Substrate with Distinct Deformability, *Mater. Des.*, 2016, **109**, p 503-510.
47. F. Meng, S. Yue, and J. Song, Quantitative Prediction of Critical Velocity and Deposition Efficiency in Cold-Spray: A Finite-Element Study, *Scr. Mater.*, 2015, **107**, p 83-87.
48. B. Yildirim, H. Yang, A. Gouldstone, and S. Müftü, Rebound Mechanics of Micrometre-Scale, Spherical Particles in High-Velocity Impacts, *Proc. R. Soc. A Math. Phys. Eng. Sci.*, 2017, **473**(2204), p 20160936.
49. G.R. Johnson and W.H. Cook, Fracture Characteristics of Three Metals Subjected to Various Strains, Strain Rates, Temperatures and Pressures, *Eng. Fract. Mech.*, 1985, **21**(1), p 31-48.
50. I. Chaban, Y. Sun, D. Veysset, K.A. Nelson, and C.A. Schuh, The Effect of Substrate Temperature on the Critical Velocity in Microparticle Impact Bonding, *Appl. Phys. Lett.*, 2021, **119**(1), p 011903.
51. M. Zain-Ul-Abdein, H. Ijaz, W. Saleem, K. Raza, A. Salmeen Bin Mahfouz, and T. Mabrouki, Finite Element Analysis of Interfacial Debonding in Copper/Diamond Composites for Thermal Management Applications, *Materials*, 2017, **10**(7), p 739.
52. S. Rahmati, R.G. Veiga, A. Zúñiga, B. Jodoin, A Numerical Approach to Study the Oxide Layer Effect on Adhesion in Cold Spray, *J. Therm. Spray Technol.*, 2021, p 1-15.
53. G. Benenati and R. Lupoi, Development of a Deposition Strategy in Cold Spray for Additive Manufacturing to Minimize Residual Stresses, *Procedia Cirp*, 2016, **55**, p 101-108.
54. S. Msolli, Z.-Q. Zhang, D.H.L. Seng, Z. Zhang, J. Guo, C. Reddy, N. Sridhar, J. Pan, B.H. Tan, and Q. Loi, An Experimentally Validated Dislocation Density Based Computational Framework for Predicting Microstructural Evolution in Cold Spray Process, *Int. J. Solids Struct.*, 2021, **225**, p 111065.
55. K. Ito and Y. Ichikawa, Microstructure Control of Cold-Sprayed Pure Iron Coatings Formed Using Mechanically Milled Powder, *Surf. Coat. Technol.*, 2019, **357**, p 129-139.
56. R. Fernandez and B. Jodoin, Cold Spray Aluminum-Alumina Cermet Coatings: Effect of Alumina Content, *J. Therm. Spray Technol.*, 2018, **27**(4), p 603-623.
57. C. Sun, X. Zhou, L. Xu, and C. Xie, Effect of Preheating on the Deformation in Cold Spraying, *Surf. Eng.*, 2018, **34**(10), p 791-799.
58. V. Lemiale, P.C. King, M. Rudman, M. Prakash, P.W. Cleary, M.Z. Jahedi, and S. Gulizia, Temperature and Strain Rate Effects in Cold Spray Investigated by Smoothed Particle Hydrodynamics, *Surf. Coat. Technol.*, 2014, **254**, p 121-130.
59. T. Schmidt, F. Gärtner, H. Assadi, and H. Kreye, Development of a Generalized Parameter Window for Cold Spray Deposition, *Acta Mater.*, 2006, **54**(3), p 729-742.
60. W. Xie, A. Alizadeh-Dehkharghani, Q. Chen, V.K. Champagne, X. Wang, A.T. Nardi, S. Kooi, S. Müftü, and J.-H. Lee, Dynamics and Extreme Plasticity of Metallic Microparticles in Supersonic Collisions, *Sci. Rep.*, 2017, **7**(1), p 5073.
61. R. Armstrong and F. Zerilli, Dislocation Mechanics Aspects of Plastic Instability and Shear Banding, *Mech. Mater.*, 1994, **17**(2-3), p 319-327.

62. F.J. Zerilli and R.W. Armstrong, Dislocation-Mechanics-Based Constitutive Relations for Material Dynamics Calculations, *J. Appl. Phys.*, 1987, **61**(5), p 1816-1825.
63. D.L. Preston, D.L. Tonks, and D.C. Wallace, Model of Plastic Deformation for Extreme Loading Conditions, *J. Appl. Phys.*, 2003, **93**(1), p 211-220.
64. R. Chakrabarty and J. Song, A Modified Johnson-Cook Material Model with Strain Gradient Plasticity Consideration for Numerical Simulation of Cold Spray Process, *Surf. Coat. Tech.*, 2020, **397**, p 125981.
65. A.A. Dehkharghani, Tuning Johnson-Cook Material Model Parameters for Impact of High Velocity, Micron Scale Aluminum Particles, Northeastern University, 2016.
66. S. Rahmati and A. Ghaei, The Use of Particle/Substrate Material Models in Simulation of Cold-Gas Dynamic-Spray Process, *J. Therm. Spray Technol.*, 2014, **23**(3), p 530-540.
67. B. Yildirim, S. Muftu, and A. Gouldstone, Modeling of High Velocity Impact of Spherical Particles, *Wear*, 2011, **270**(9-10), p 703-713.
68. G.S. Schajer and M. Steinzig, Full-Field Calculation of Hole Drilling Residual Stresses from Electronic Speckle Pattern Interferometry Data, *Exp. Mech.*, 2005, **45**, p 526-532.
69. W. Li, K. Yang, D. Zhang, X. Zhou, and X. Guo, Interface Behavior of Particles Upon Impacting During Cold Spraying of Cu/Ni/Al Mixture, *Mater. Des.*, 2016, **95**, p 237-246.
70. V. Luzin, K. Spencer, M. Zhang, N. Matthews, J. Davis, and M. Saleh, Residual Stresses in Cold Spray Coatings, *Cold-Spray Coatings*. P. Cavaliere Ed., Springer, Cham, 2018, p 451-480
71. E. Lin, I. Nault, O.C. Ozdemir, V.K. Champagne, A. Nardi, and S. Müftü, Thermo-Mechanical Deformation History and the Residual Stress Distribution in Cold Spray, *J. Therm. Spray Technol.*, 2020, **29**(6), p 1424-1436.

**Publisher's Note** Springer Nature remains neutral with regard to jurisdictional claims in published maps and institutional affiliations.

Springer Nature or its licensor (e.g. a society or other partner) holds exclusive rights to this article under a publishing agreement with the author(s) or other rightsholder(s); author self-archiving of the accepted manuscript version of this article is solely governed by the terms of such publishing agreement and applicable law.